Higher-Order Simulations of Interactional Aerodynamics on Full Helicopter Configurations Using a Hamiltonian Strand Approach

Jannik Petermann[*,1] **Yong Su Jung**[†,2] **James D. Baeder**[‡,2] **Jürgen Rauleder**[§,1]

Time-accurate numerical predictions of the interactional aerodynamics between NASA's generic ROBIN fuselage and its four-bladed rotor were performed using the recently developed RANS solver HAMSTR. The fifth-order WENO reconstruction scheme, the third-order MUSCL scheme, a second-order temporal resolution, and the Spalart–Allmaras turbulence model were used. Three-dimensional volume meshes were created in a robust manner from two-dimensional unstructured surface grids using Hamiltonian paths and strands on nearbody domains. Grid connectivity was established between nearbody and background domains in an overset fashion. Two previously researched operational conditions were reproduced, i.e., a near-hover case and a medium-speed forward flight case at an advance ratio of $\mu = 0.151$. The results were compared with various experimental and numerical references and were found to be in good agreement with both. The comparison included the analysis of the rotor wake structure, tip vortex trajectories and strength, steady and dynamic fuselage pressure distributions in longitudinal and lateral directions, and rotor inflow predictions.

NOMENCLATURE

α_s	shaft tilt angle
β_0	blade coning angle
γ_f	fuselage yaw angle
λ	perpendicular rotor inflow
ξ,η,ζ	cell local coordinate system
ρ	fluid density
μ	advance ratio, $V_\infty/(\Omega R)$
τ	pseudo time
ω	vorticity magnitude
Θ_0	collective pitch angle
Θ_{1C}	lateral cyclic pitch
Θ_{1S}	longitudinal cyclic pitch
Ψ_b	blade azimuth angle
Ψ_w	wake age
Ω	rotor rotational frequency
n	physical time-level
p	static pressure
$\tilde{p}$	pseudo time-level
t	physical time
u,v,w	velocity components
x,y,z	global coordinates
A_{Roe}	Roe's flux Jacobian
C_P	pressure coefficient, $(p-p_\infty)/\frac{1}{2}\rho V_\infty^2$
C_P^*	modified pressure coefficient, $(p-p_\infty)/\rho(\Omega R)^2\cdot 100$
C_T	thrust coefficient, $T/\rho\pi R^2(\Omega R)^2$
F,G,H	flux vectors
I	identity matrix
L	reference length
M	Mach number
Q	vector of conservative variables
R	rotor radius
$\tilde{R}$	residual
S_i	surface area
V_∞	far-field velocity

1. INTRODUCTION

Many aspects of a helicopter's performance strongly depend on its aerodynamic behavior. Crew endurance and passenger comfort are significantly influenced by noise and vibrations in the fuselage. Hence, the interaction between rotor wake and fuselage has been of interest in many experimental and computational studies. Due to its vortical nature, the precise capturing of the wake is one of the crucial aspects to accurately predict its influence on the cabin. For better prediction of the interactional aerodynamic phenomena, an efficient and accurate approach is desirable in

---

[*] Graduate Student: jannik.petermann@tum.de

[†] Graduate Research Assistant: jung9053@umd.edu

[‡] Professor: baeder@umd.edu

[§] Lecturer: juergen.rauleder@tum.de

[1] Institute of Helicopter Technology
Technical University of Munich, Germany

[2] Department of Aerospace Engineering
University of Maryland at College Park, MD, USA

Presented at the 44th European Rotorcraft Forum, Delft, Netherlands, September 18–20, 2018. Copyright ©2018 by the authors except where noted. All rights reserved. Published by CEAS with permission.

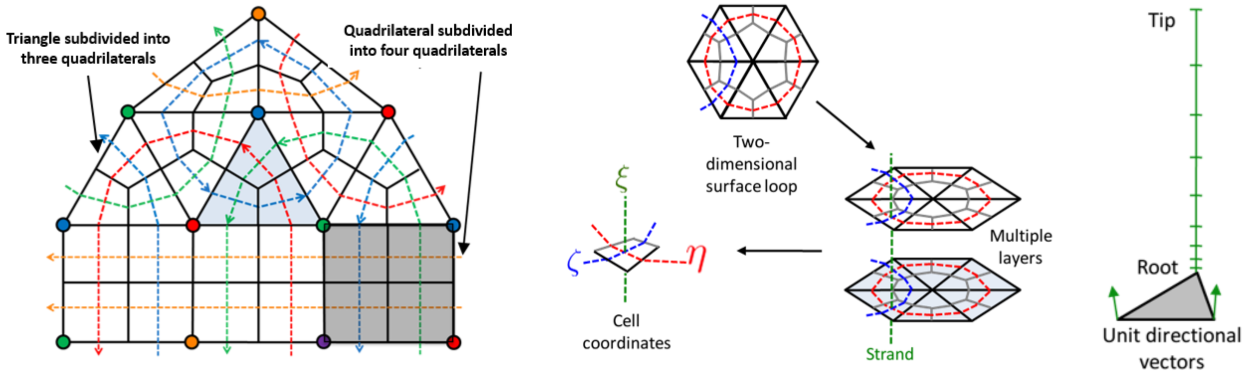

(a) Mixed triangles and quadrilaterals (b) Construction of strands (c) Strand template

Fig. 1: Hamiltonian paths and strands grids in wall-normal direction (adapted from (Ref. 1))

simulations by using line-implicit methods and high-order-type reconstruction which are typically available only on structured grids.

Since, in general, the construction of fully structured grids requires much attention and effort for complex geometries, the use of unstructured grids has been the method of choice in past computational research on this topic (Refs. 2, 3). The University of Maryland has developed a new approach to create features of a structured domain from easy-to-create, fully unstructured surface meshes, using so-called Hamiltonian paths and strands (Refs. 4, 5). Various smaller test cases on simple geometries and wing sections have been conducted in the past (Ref. 4). The present paper presents an extension of the previous work to a full helicopter configuration, comprised of a four-bladed rotor and NASA's ROBIN fuselage (Ref. 6). The latter has been tested extensively, numerically and experimentally, and hence provides a large range of validation references.

The objective of the research was to assess the capabilities of the new software with regard to simulating full helicopter configurations and provide information on the sensitivity of the current solution with regard to different numerical strategies and treatments. A comprehensive comparison and validation of the current results on the ROBIN configuration with various experiments and numerical studies was performed. This included the analysis of the rotor wake structure, the wake trajectory and intensity, steady and dynamic fuselage surface pressure distributions, and rotor inflow prediction.

2. METHODOLOGY

Hamiltonian paths

A solution framework using Hamiltonian paths and strand grids (HAMSTR) is used for three-dimensional flows on overset and hybrid meshes. The methodology creates a volume mesh starting from an unstructured surface mesh that can comprise mixed triangular-quadrilateral elements. "Linelets" through the meshes are found in a robust manner and the solver uses line-based schemes along these linelets, similar to a structured solver (Ref. 4).

The underlying principle of creating linelets is realized through the sub-division of the triangles or quadrilaterals in an unstructured grid into all-quadrilaterals. The subdivision process is explained using the schematic presented in Fig. 1 (a). The process of path identification (referred to as chains or loops) is robust as each edge only belongs to one chain. Figure 1 (a) shows the resulting paths that are formed from a mixed triangular–quadrilateral mesh. The generated Hamiltonian loops are either closed or open end at the boundary. To extend the formulation to three dimensions, strand-based grids have been employed in the present work, which provide a structure in the wall-normal direction as shown in Fig. 1 (b) and (c). Consequently, these strand grids allow for line-implicit methods and stencil-based reconstruction to be used along their spatial direction. The construction of hexahedral layers from initial triangular mesh elements is shown in Fig. 1 (b). Each cell therefore has two Hamiltonian path lines and one wall-normal strand line for a total of three "cell-coordinate" directions.

The described technique yields some advantages over traditional unstructured methods. First, linelets are clearly identified in all spatial directions, which allows the use of both line implicit-methods and stencil-based discretization along the lines. Second, the connectivity of the Hamiltonian paths is preserved across the multiple layers along the strand grid, saving memory and computational time, and finally, the methodology is readily amenable to parallelization techniques.

The near-body Hamiltonian/Strand grid and off-body Cartesian grid are connected in an overset fashion using TIOGA (Topology Independent Overset Grid Assembler) (Ref. 7). The approach enables the consideration of relative motion between the rotating blades and the stationary fuselage in the current simulations and to capture the aerodynamic phenomena better by connecting finer nested meshes in regions of interest.

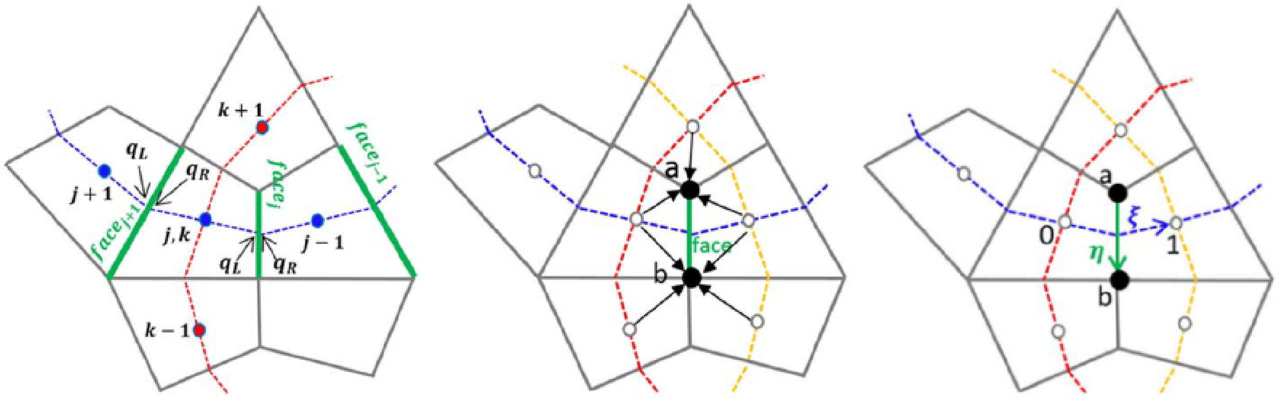

(a) Numbering scheme (b) Average at node points (c) Velocity gradients at faces

Fig. 2: Face numbering scheme, node evaluation, and stream-wise and cross-term flux evaluation in HAMSTR (adapted from (Ref. 4))

Governing equations

The present work uses the unsteady, three-dimensional, compressible Navier–Stokes equations, which can be expressed as

$$\frac{\partial \mathbf{Q}}{\partial t} + \nabla \cdot \left[(\mathbf{F_C} - \mathbf{F_V}), (\mathbf{G_C} - \mathbf{G_V}), (\mathbf{H_C} - \mathbf{H_V}) \right] = 0 \quad (1)$$

where $\mathbf{Q}$ represents the vector of the conserved variables, i.e., density, momentum, and total energy $[\rho, \rho u, \rho v, \rho w, e]^T$ and $\mathbf{F}$, $\mathbf{G}$, and $\mathbf{H}$ represent the three-dimensional convective and viscous fluxes in each spacial direction with the indices “C” and “V,” respectively. A finite volume formulation using implicit discretization and a first-order backwards time stepping scheme, yields

$$\frac{\mathbf{Q}^{n+1} - \mathbf{Q}^n}{\Delta t} = -\sum_{i=0}^{N} \mathbf{F}(\mathbf{Q}^{n+1}) \cdot \Delta S_i \quad (2)$$

The first-order linearization of equation (2) results in a system of algebraic equations, which must be inverted at each iteration in order to evolve the solution

$$\left[\frac{\mathbf{I}}{\Delta t} + \frac{\partial \mathbf{F}}{\partial \mathbf{Q}} \right] \left(\mathbf{Q}^{n+1} - \mathbf{Q}^n \right) = -\tilde{\mathbf{R}}(\mathbf{Q}^n) \quad (3)$$

The right hand side (RHS) of this equation is called the solution residual $\tilde{R}$, evaluated at time-level n. The implicit operator was solved using the diagonally dominant line Gauss Seidel (DDLGS) technique (Ref. 4).

For time-accurate solutions, a dual time stepping technique, combined with first- and second-order backward time stepping methods are applied, resulting in the formulation

$$\left[\frac{\mathbf{I}}{\Delta \tau} + \frac{\mathbf{I}}{\frac{2}{3}\Delta t} + \left(\frac{\partial \tilde{\mathbf{R}}}{\partial \mathbf{Q}} \right)^{\tilde{p}} \right] \Delta \mathbf{Q}^{\tilde{p}} = - \left[\frac{3\mathbf{Q}^p - 4\mathbf{Q}^n + \mathbf{Q}^{n-1}}{2\Delta t} + \tilde{\mathbf{R}}(\mathbf{Q}^p) \right] \quad (4)$$

where the sub-iteration level in pseudo-time τ is denominated by the letter $\tilde{p}$ and the term Δt^* equals

$$\Delta t^* = \frac{\frac{2}{3}\Delta t}{\frac{2\Delta t}{3\Delta \tau} + 1} \quad (5)$$

In HAMSTR, Roe’s approximate Riemann solver (Ref. 8) is applied using $\mathbf{Q}^{\mathrm{R}}$ and $\mathbf{Q}^{\mathrm{L}}$ as left and right states at a given face

$$\mathbf{F}_C = \frac{\mathbf{F}(\mathbf{Q}^L) + \mathbf{F}(\mathbf{Q}^R)}{2} - |A_{Roe}| \frac{\mathbf{Q}^R - \mathbf{Q}^L}{2} \quad (6)$$

A low Mach-number correction by Rieper (Ref. 9) is used within the Roe’s scheme. Spatial reconstruction, implicit schemes, and the computation of left and right states using gradients of field variables are performed along the Hamiltonian paths and strands. In the present work, the third-order Monotone Upstream Conservative Limited (MUSCL) scheme with Koren’s limiter (Ref. 10) and the fifth-order Weighted Essentially Non-Oscillatory (WENO) (Ref. 11) scheme were applied to calculate inviscid fluxes.

The viscous fluxes were obtained from velocity gradient calculations using second-order central difference discretizations. The node values Φ_a and Φ_b are found by averaging the values at cell centers, as shown in Fig. 2 (b). For example, in two dimensions, the streamwise and cross-term evaluation of the velocity gradients along the linelets is depicted in Fig. 2 (c). This leads to the formulations for the spacial gradients of the velocity components, which are represented by Φ (Ref. 4)

$$\frac{\partial \Phi}{\partial x} = \xi_x \frac{\partial \Phi}{\partial \xi} + \eta_x \frac{\partial \Phi}{\partial \eta} \quad (7)$$

$$\frac{\partial \Phi}{\partial y} = \xi_y \frac{\partial \Phi}{\partial \xi} + \eta_y \frac{\partial \Phi}{\partial \eta} \quad (8)$$

where $\Phi_\xi = \Phi_1 - \Phi_0$, $\Phi_\eta = \Phi_b - \Phi_a$, $x_\xi = x_1 - x_0$, $y_\xi = y_1 - y_0$, $x_\eta = x_b - x_a$, and $y_\eta = y_b - y_a$.

To account for the effects of turbulence in the current RANS (Reynolds-Averaged Navier–Stokes) simulations, the Spalart–Allmaras (SA) turbulence model was

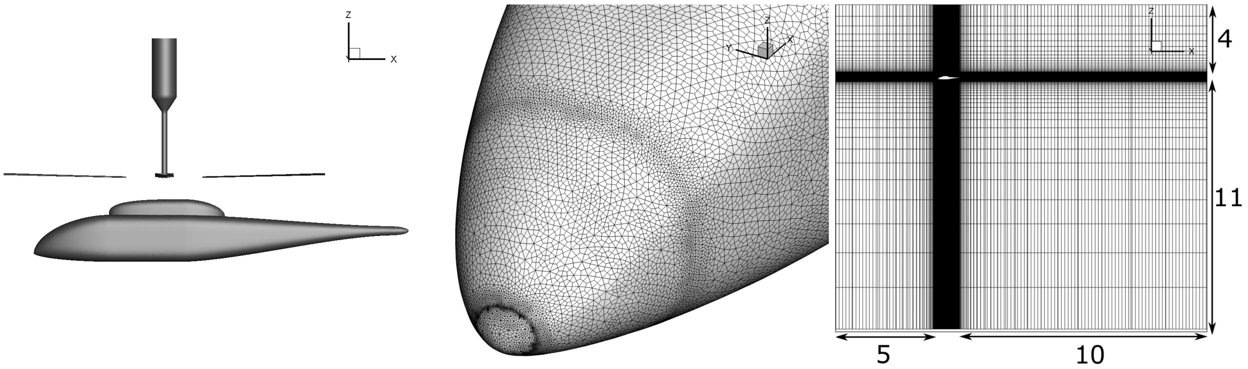

(a) Full rotor–fuselage configuration with model of upper support structure (b) Fuselage surface mesh based on triangles after subdivision (c) Domain size in multiples of fuselage length

Fig. 3: ROBIN model, surface mesh, and domain size

used (Ref. 12). A diagonally dominant alternating direction implicit scheme computed the correlating transport equation (Ref. 4). In this study, the delayed detached eddy simulation (DDES) method was integrated to the RANS/SA model framework in the case of massive separated flow (Ref. 4). As proposed by Spalart et al. (Ref. 13), it better preserves the RANS mode within the boundary layer by using a "f_d function" in the DES length scale $\tilde{d}$

$$\tilde{d} \equiv d - f_d \max(0, d - C_{\mathrm{DES}}\Delta) \qquad C_{\mathrm{DES}} = 0.65 \qquad (9)$$

where d and Δ denote the wall-normal distance in the destruction term of the SA model and subgrid length scale, respectively. The eddy viscosity is governed by the length scale $\tilde{d}$ with the subgrid length scale corrected to account for anisotropy in the grid, which was proposed by Scotti et al. (Ref. 14). Calculations using the software GARFIELD used the maximum local grid spacing as the length scale, since only used for Cartesian off-body meshes.

3. MODEL DESCRIPTION

The aircraft model that was investigated in this paper had originally been defined by NASA and consists of the main fuselage and a pylon that represents an engine fairing. Both geometric features are described analytically and the corresponding parameters were taken from reference (Ref. 6). The -8° twisted and untapered blades consisted entirely of NACA 0012 airfoil sections with a chord length of 0.0663 m. The rotor radius was 0.86 m, the root cut-out was 24% and the blade operational tip Mach-number in hover was 0.53. When viewed from above, the rotor rotated in counter-clockwise direction and the zero azimuth position was located above the tail of the fuselage. The reference length of one meter was defined as half of the fuselage length. According to the original experimental report, due to manufacturing issues, a fuselage yaw of 1.2° and a shift of the rotor hub of two inches to starboard had to be taken into account upon remodeling the experiment (Ref. 6).

Two different advance ratios μ were investigated: a near-hover case with $\mu = 0.012$, and a medium-speed forward flight case with $\mu = 0.15$. In the latter, a shaft tilt angle of $\alpha = -3^\circ$ was applied to the rotor. Due to the rotor trim, blade flapping was avoided and only a stationary coning angle of $\beta_{0,\mathrm{hover}} = 1.3^\circ$ and $\beta_{0,\mathrm{forward}} = 1.7^\circ$ were used in the current simulations. The collective and cyclic pitch settings of the experiment were found to be inadequate for the numerical simulations, and due to the lack of trim coupling in the current HAMSTR software, the trim results were taken from Lee (Ref. 2) and slightly modified to fit the according averaged experimental thrust coefficient for each operational condition. Table 1 shows the most important settings that were applied in the present work.

The full configuration, a detail of the fuselage surface mesh, and the domain dimensions are shown in Fig. 3. The constant grid spacing of the background domain around the blades and the body was 10% of the blade chord length. A stretching of the grid towards the domain borders was applied to reduce the number of volume cells, which was 18 million for the background grid and 39.1 million in total.

Analog to the research of previous studies, no hub geometry was modeled in order to obtain comparable results and since complex geometries were difficult to create with current meshing capabilities within the HAMSTR software. In contrast to the experiment, only a support structure for the rotor was modeled. The rear support beam of the fuselage was not accounted for, because of issues with the overset grid connectivity and the nearbody mesh generation due to acute angles and intersecting strands, respectively.

Table 1: HAMSTR simulation settings

μ	[-]	0.012	0.15
M_∞	[-]	0.0064	0.08
α_s	[°]	0.0	-3.0
β_0	[°]	1.3	1.7
γ_f	[°]	1.2	1.2
Θ_0	[°]	8.55	6.30
Θ_{1C}	[°]	0.10	2.20
Θ_{1S}	[°]	-0.20	-2.00

4. RESULTS AND DISCUSSION

Near-hover case

The nominal experimental thrust coefficient for all cases was 0.0064, which was matched with a difference of $+2.2\%$ in the near-hover case. A timestep size of one degree per iteration with 20 subiterations was applied after convergence and the WENO reconstruction scheme defined by Jiang and Shu (Ref. 11) was used. The pressure history was taken from 11.5 to 12.5 rotor revolutions. More iterations compared to other cases were necessary due to the interaction of the starting vortex with the rotor from about four to seven rotor revolutions.

Wake visualization The rotor wake of the near-hover case is shown in Fig. 4 using the Q-criterion of $Q = 2.5 \cdot 10^{-4}$ to visualize the wake structures by iso-surfaces. The color coding uses the vertical velocity to indicate the intensity and rotational orientation of a vortex filament. The phenomenon of secondary unstable vortex structures was observed, which arised from the bottom to the top of the tip vortex helix after about four rotor revolutions. However, these perturbations only seem to have little effect on other assessed quantities, such as the surface pressure distribution (Ref. 15). The lack of viscous damping from the inviscid treatment of the background potentially supported the growth of these structures (Ref. 15).

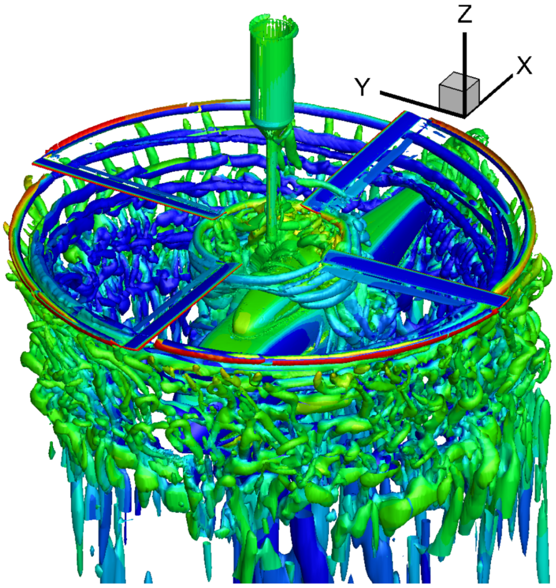

Fig. 4: Rotor wake isometric view at $\mu = 0.012$

A comparison between the MUSCL and WENO reconstruction schemes at one degree timestep size is shown in Fig. 5. The vorticity magnitude was visualized at the fuselage centerline section to show the differences in the wake resolution. The tip vortices along the trajectories at nose and tail of the fuselage were less distinct in case of the MUSCL scheme compared to the WENO scheme. The vortices on the tail merged to a larger vortex sheet in the MUSCL solution, rather than remaining independent from each other as seen using the WENO reconstruction method.

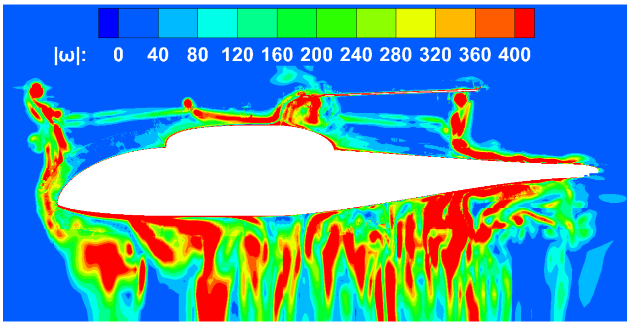

(a) MUSCL

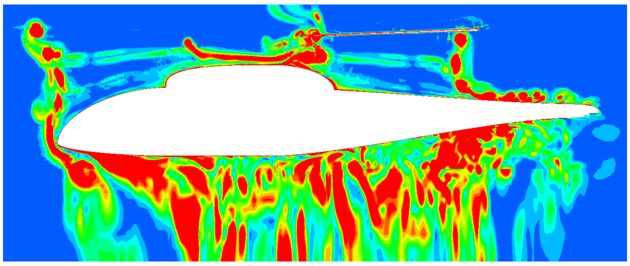

(b) WENO

Fig. 5: Vorticity magnitude [1/s] between MUSCL and WENO scheme at $\mu = 0.012$

Fuselage centerline pressure evaluation Dynamic surface pressure measurements were performed experimentally for 360 degrees and the signal of each transducer was averaged over 30 rotor revolutions (Ref. 6). The so-called "Isolated Rotor Test System" (IRTS) was used in this experimental setup, which was attached to a support structure that was mounted at the ceiling of the test facility; see Fig. 3 (a). The positions of the pressure transducer locations on the suface of the ROBIN fuselage in longitudinal and lateral directions are shown in Fig. 6. The exact orifice positions are listed in the experimental report (Ref. 6).

The static pressure was nondimensionalized using the rotor tip speed instead of the far-field velocity. For better visualization, the resulting pressure coefficient was multiplied by the factor 100, as shown in Eq. 10

$$C_p^* = \frac{p - p_\infty}{\rho(\Omega R)^2} \cdot 100 \tag{10}$$

Due to an asynchronism between the experimental pressure recording and the actual blade position, the experimental data lagged between 28° at locations on the front and 35° at the tail of the helicopter (Ref. 6). To match with the numerical results, the data was shifted by 28 degrees on all displayed dynamic plots in the present paper.

While the current results showed a slight phase variation at transducer position D8 in Fig. 7 at particular azimuth angles, the amplitude of the pressure oscillations and the

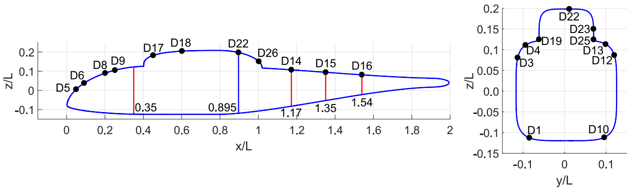

Fig. 6: Longitudinal (left) and lateral (right) pressure transducer locations at $y/L = 0.007$ and $x/L = 0.895$, respectively

mean pressure matched the experiment well. The previous results by Lee (Ref. 2) showed slightly increased amplitudes and predicted a lower minimum pressure. None of the points on the nose of the fuselage were in direct interaction with the blade tip or root vortices. Due to the shape of the pressure characteristics, the blade passing event was the major influencing factor. Analogous to the medium-speed forward flight case shown later, the experimental trends exhibited unsteady behavior, leading to unequally strong pressure amplitudes throughout one rotor revolution. The error resulted from small differences of the blade geometries and weight distributions used in the experiments (Ref. 6).

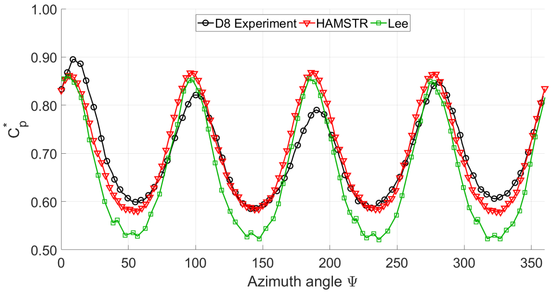

Fig. 7: C_p^* at pressure transducer D8 and $\mu = 0.012$

Transducer location D15 is shown in Fig. 8. The pressure recordings showed a good correlation of the current data and the experiment. Both numerical results predicted the magnitude of the experiment well, while they showed a small phase offset of about six degrees. This fits well to the reported lag difference between bow and tail, which was not accounted for in the present plots.

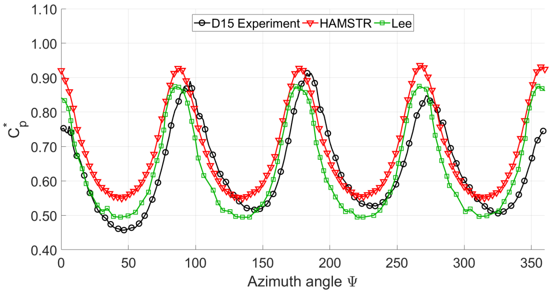

Fig. 8: C_p^* at pressure transducer D15 and $\mu = 0.012$

Figure 9 shows the steady modified pressure coefficient for the fuselage centerline, obtained from averaging the dynamic pressure over 360 degrees of rotor rotation. Unfortunately, no numerical benchmark was found for comparison. The simulation captured the general trend of the experiment (Ref. 6) well in terms of magnitude and shape. However, a slight axial offset was observed, especially on the fuselage front part. At the two leftmost pressure transducers on the nose of the fuselage (D5 and D6), the current mean pressures were lower than the experiment, while both curves approached each other at D8. The same trend was observed in the previous numerical data by Lee. A similar trend was obtained for the last three pressure transducers on the fuselage tail boom.

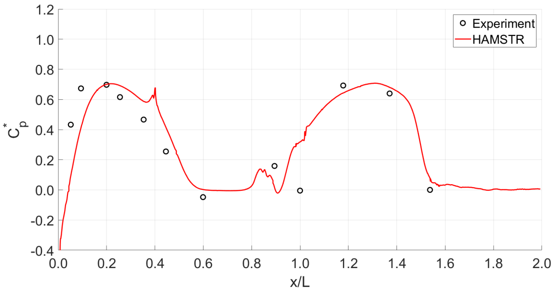

Fig. 9: Fuselage centerline steady C_p^* at $\mu = 0.012$

A secondary localized pressure excursion was found at about $x/L = 0.9$ and it is assumed that this event was caused by the conglomeration of root vortices and other aerodynamic wake residue in this region. While the simulation was capable of determining the peak, it was still slightly shifted to smaller axial stations. It should be noted that the lateral dynamic pressure measurements were taken in this region and, hence, differences between simulation and experiment can be expected. Furthermore, the coarse distribution of pressure transducers might be misleading when comparing to more continuous numerical results.

Fuselage circumferential pressure evaluation The two dynamic pressure curves of transducers D19 and D25 are shown in Figs. 10 and 11, respectively, and the two locations are counterparts at each side of the fuselage. While the current and previous numerical results agreed well with the experiment in terms of mean pressure and amplitude on the port side (D19), both were numerically overpredicted on starboard (D25). However, the current solution showed some peaks that agreed much better with the experiment than others, indicating the influence of the unsteady wake.

The ten available circumferential pressure transducers showed stronger unsteady behavior of the experimental pressure curves compared to the centerline measurements. Since the axial station of the lateral transducers was situated within the root cut-out at $x/L = 0.895$, the influence of the blade passing event decreased, while the effect of the wake impact increased. The unsteady and rather chaotic nature of the latter took effect on the transient pressure, which became more irregular. Since only the recording from one revolution is displayed for the numerical results,

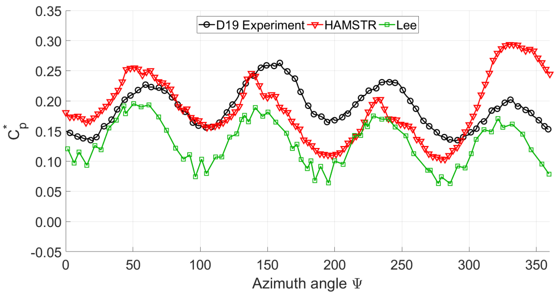

Fig. 10: C_p^* at pressure transducer D19 and $\mu = 0.012$

it can be assumed that an average of the pressure measurement of one particular orifice from several revolutions would balance some of the unsteady peaks and, thus, improve the result considerably.

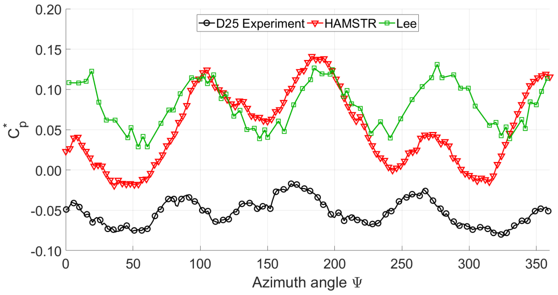

Fig. 11: C_p^* at pressure transducer D25 and $\mu = 0.012$

In Fig. 12 at $x/L = 0.35$, the current result was practically identical to the previous numerical solution by Lee on the upper half of the fuselage at both sides and deviated from it on the lower half. This difference might be due to the current turbulent nearbody treatment compared to the inviscid setting by Lee. While both numerical solutions seem to overshoot the experimental curve in the upper half, another experimental pressure probe at $z/L = 0.07$ might show a similar tendency, i.e. the coarse distribution of pressure transducers may be misleading.

On the lower part of the port side, the current results approximated the experiment better, although the oscillating behavior was not reflected in the latter. While the trend in both numerical results was in opposite direction on the lower half, this was not observed on starboard. Here, the current results showed the same tendency as the previously simulated pressures, with decreased magnitude in the lower half. In general, the deviation between the numerics and the experiment was greater on the side of the advancing blade, i.e., starboard. However, a better comparison could be done if more experimental probes were available, in order to create a more precise lateral pressure profile.

At the axial station further downstream at $x/L = 1.17$ shown in Fig. 13, the current results showed very good agreement on the retreating side (port side) in the lower half, while the previous results clearly overpredicted the negative pressure. On the upper half, both numerical solutions came close to the experimental recordings but still showed smaller volumes of suction pressure. On starboard, a reversed behavior of current and previous numerical result was observed, while both solutions followed the experimental chart. However, the current simulation appeared to approximate the real conditions slightly better than the previous one by Lee, except for the top part, where too low pressures were predicted.

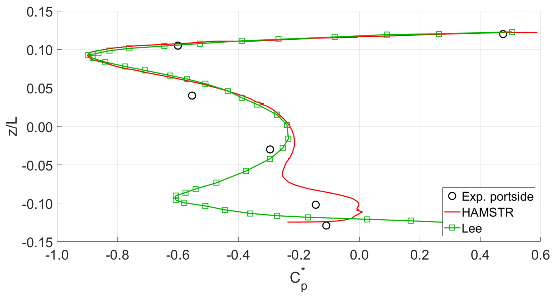

(a) Port

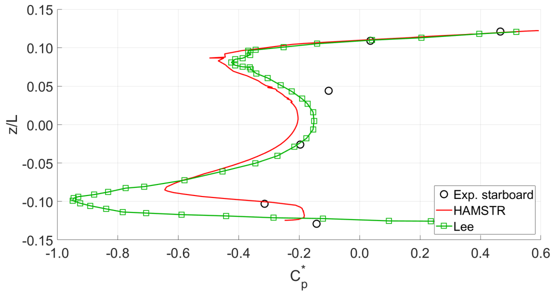

(b) Starboard

Fig. 12: Lateral steady C_p^* at $x/L = 0.35$ and $\mu = 0.012$

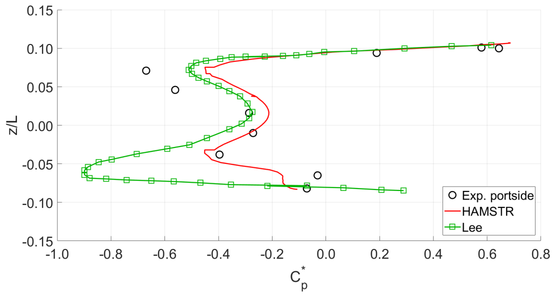

(a) Port

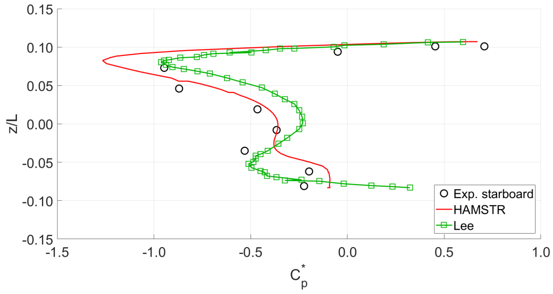

(b) Starboard

Fig. 13: Lateral steady C_p^* at $x/L = 1.17$ and $\mu = 0.012$

Effects of grid resolution and numerical schemes

Further investigations concerning the solution quality of different numerical settings were performed using the near-hover case, since vortex–fuselage interaction is dominant in this flight condition. The tip vortex intensity was visualized using the vertical velocity component, w. The blade tip vortices around zero azimuth angle, as well as the vortices shortly before and after impact on the fuselage tail boom at the same azimuthal position were selected to assess the accuracy of the reconstruction schemes, i.e, the MUSCL scheme using Koren's limiter (Ref. 10), the WENO scheme as defined by Jiang and Shu (WENO-JS) (Ref. 11), and the WENO scheme using improved weights proposed by Borges et al. (WENO-Z) (Ref. 16). Furthermore, different timestep sizes of 1.0° and 0.25° per iteration, and a refined grid spacing of 0.05c instead of 0.1c were assessed at these locations.

Since the refined grid spacing led to a large number of cells, only a small part of the entire model was altered, ranging from above the blade to below the tail of the fuselage at zero azimuth angle. This domain was nested into a second grid with the standard spacing of 10% chord length. A third domain with a very coarse grid completed the setup. The background domains were assigned to the GPU-accelerated flow solver GARFIELD (Ref. 17) to reduce the computational cost. Compared to the standard cases with an inviscid flow assumption on the background domain, fully turbulent flow (SA-DDES) was used on the background for the refined grid case as well.

In Fig. 14 (a), the rear view of the wake structures of the ROBIN model is shown using the Q-criterion, the refined nested grid, the WENO scheme with Borges' weights, and a fully turbulent background. In Fig. 14 (b), the standard grid (0.1c), the WENO scheme by Jiang and Shu, and an inviscid treatment of the background were used. The color coding uses the vertical momentum component in dimensionless form, which was obtained using the far-field density times the speed of sound as denominator. In both cases, a timestep size of one degree per iteration was used. The comparison of Fig. 14 (a) and (b) shows a strong decrease of the secondary vortex filaments in (a). Since it is assumed that these structures mostly arise from numerical errors, the additional physical damping caused by the viscous background might be the reason for their reduction. Furthermore, the diameter and indicated vertical momentum of the trailed tip vortices changes abruptly after entering the refined grid section. Assessment of the fuselage surface pressure distribution, however, showed that no superior results were obtained in this case.

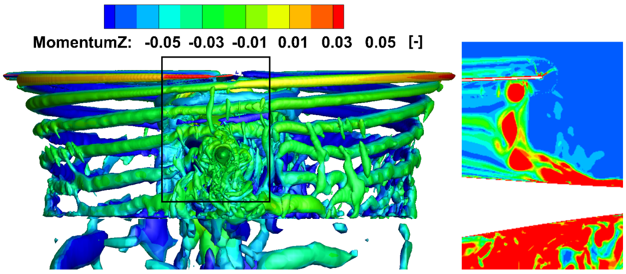

(a) Refined nested grid (black rectangle), WENO-Z, fully turbulent background

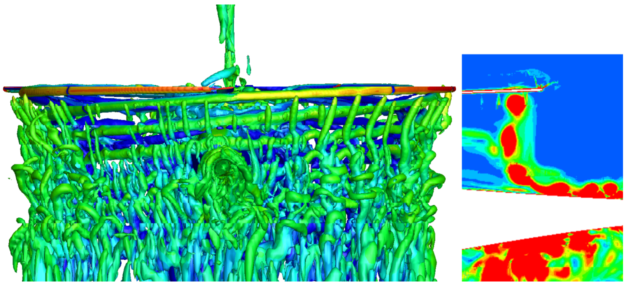

(b) Standard grid, WENO-JS, inviscid background

Fig. 14: Rear view of near-hover rotor wake using iso-surfaces at $Q = 2.5 \cdot 10^{-4}$ and centerline section of vorticity magnitude ω between 0 and 400 s^{-1}

Figure 15 shows an instantaneous tip vortex comparison on the background grid at a distance of five chord lengths behind the trailing edge of the rotor blade at zero azimuth angle. The vortex core was determined visually using the vorticity magnitude and the quarter-degree timestep size solution, and the exact coordinates were evaluated in each of the remaining cases as well. While the investigation of the vortex intensity on the blade's nearbody domain at 0.5c behind the trailing edge revealed no difference between either of the assessed cases, the viscous damping of the background in the latest setup led to a slight reduction of the vertical velocity in the tip vortex further away from the trailing edge. However, no spacial stretching or displacement was observed.

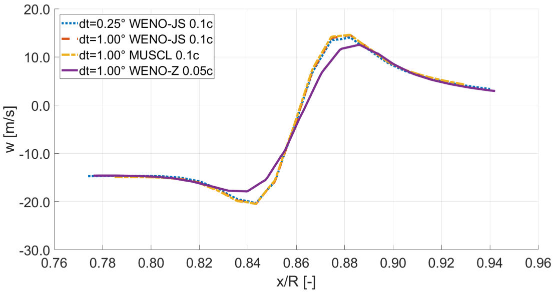

Fig. 15: Near-hover tip vortex intensity comparison in terms of vertical velocity five chord lengths behind trailing edge ($\Psi_w \approx 23.9°$)

Since the vortices only spent a short time on the background domain, before entering the unaltered fuselage nearbody domain, only a small impact from the additional viscous treatment of the background compared to the previously inviscid formulation is found in Fig. 16. The result using the WENO formula in combination with Borges' weights shows similar conduct as the other WENO scheme. The case using the MUSCL scheme shows greater deviations from the other results.

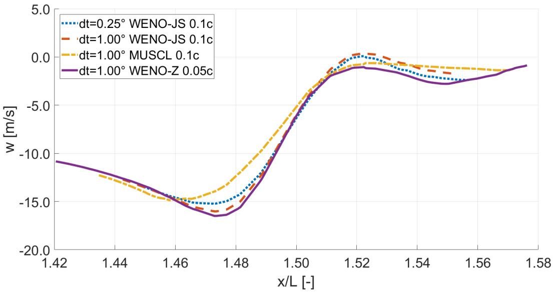

Fig. 16: Near-hover tip vortex intensity comparison in terms of vertical velocity shortly before impact on fuselage (Ψ_w= 270°)

Greater differences were found after the impact of the tip vortex on the tail boom, as shown in Fig. 17. Again, the case where the MUSCL scheme was applied differed most from the other results, which correlates to the observations in Fig. 5. No difference of the reduced timestep size in combination with the original WENO formulation by Jiang and Shu (JS) was asserted concerning the tip vortex intensity or tip vortex location. The WENO scheme using Borges' weights (Z), on the contrary, predicted a reduced vortex intensity and in parts stretched vortex cores, similar to the MUSCL case. Since there were no experimental data to validate these numerical results, it was not clear which scheme and weighting function provided the best approximation of the real flow physical conditions.

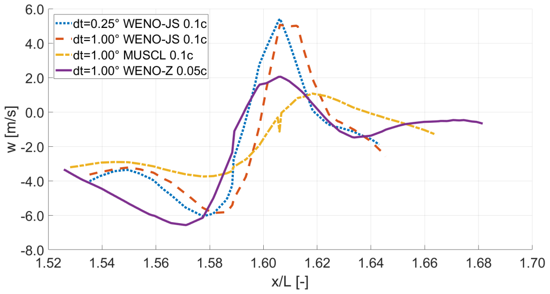

Fig. 17: Near-hover tip vortex intensity comparison in terms of vertical velocity shortly after impact on fuselage (Ψ_w= 360°)

Medium-speed forward flight case at $\mu = 0.151$

This test condition had been the subject of most of the previous numerical studies and, thus, a variety of numerical techniques can be compared for their performance. The present unsteady simulations using HAMSTR were run using a one-degree timestep size, 20 subiterations, and the WENO scheme by Jiang and Shu (Ref. 11). The dynamic pressure coefficients were recorded from 7.25 to 8.25 rotor revolutions after convergence had been achieved.

Rotor disk inflow The inflow characteristics were experimentally obtained on a ROBIN model with an attached

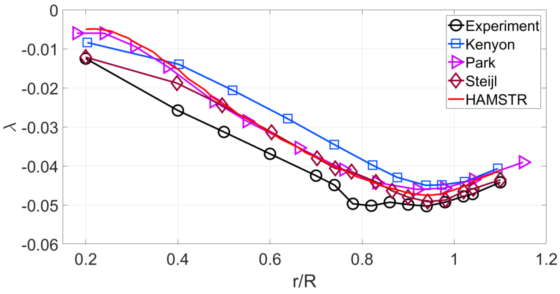

(a) $\Psi = 0°$

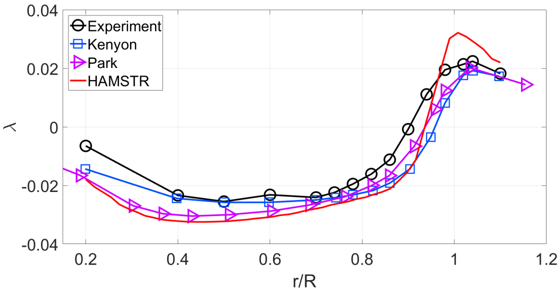

(b) $\Psi = 90°$

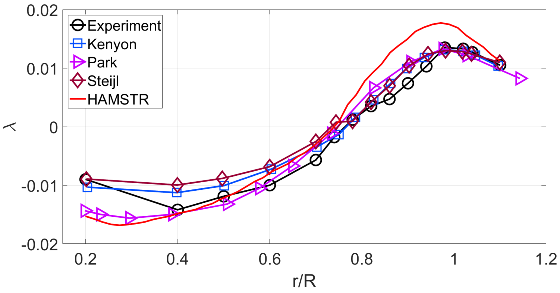

(c) $\Psi = 180°$

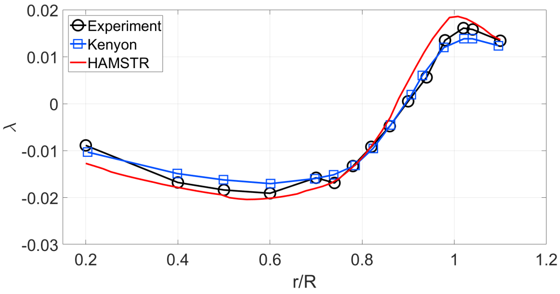

(d) $\Psi = 240°$

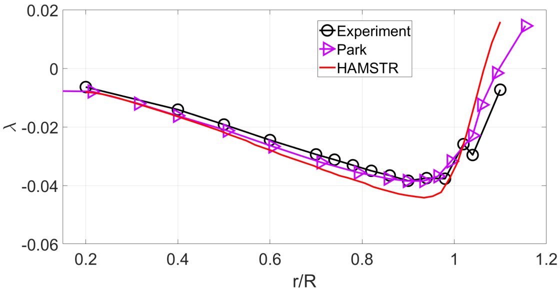

(e) $\Psi = 300°$

Fig. 18: Averaged perpendicular rotor inflow λ at different azimuthal positions at an advance ratio of 0.151

rotor, i.e., no ceiling-mounted support beam was present (Ref. 18). Hence, the comparison for the perpendicular inflow shown in Fig. 18 used a numerical model which did not contain the upper support beam. To compare to the experiment, the velocity component perpendicular to the tip path plane (TPP) was obtained in a distance of 1.15 chord lengths above the TPP and nondimensionalized with the rotor tip speed. A negative sign of the dimensionless perpendicular velocity corresponds to an inflow into the rotor plane, whereas a positive sign indicates an upwash through the rotor plane. The shown results are an arithmetic mean from a quarter of a rotor revolution, consisting of nine azimuthal blade locations.

In general, Fig. 18 shows a good agreement of the HAMSTR results with both experiment and other numerical rotor inflow analyses. The upwash at the blade tip and the inflow at radial positions closer to the rotor hub were slightly overpredicted at all investigated azimuth positions greater than zero. Since the integrated thrust coefficient matched the experiments, the local deviations of the inflow were most likely caused by the different cyclic pitch settings. Superior behavior of any particular numerical result was not observed.

Wake visualization and wake trajectory In Fig. 19 the Q-criterion with an iso-surface value of $Q = 2.5 \cdot 10^{-4}$ was applied to visualize the wake structures surrounding the ROBIN model. The same color coding as in case of Fig. 14 was used.

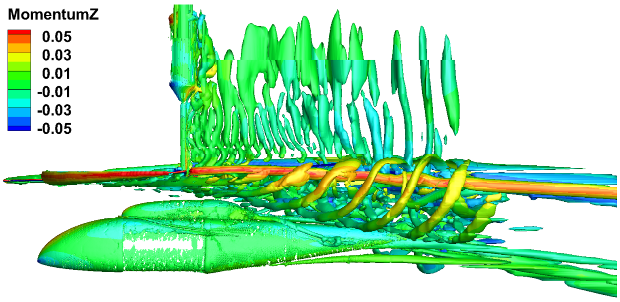

(a) Side view

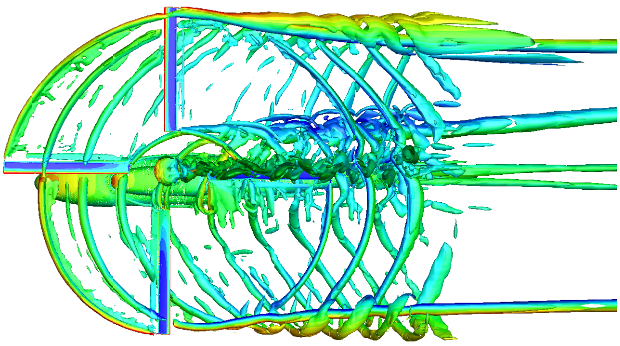

(b) Top view

Fig. 19: Wake visualization using Q-criterion isosurfaces at an advance ratio of 0.151

Vortex sheets trailed behind the rotor blades appear at this setting, and further reduction of the Q-criterion would reduce clarity in the images. Besides the vortex shedding behind the upper support beam, Fig. 19 (a) shows the development of two distinct vortices, which are attached to the fuselage and emerge from the intersections between the main body and the pylon at the front and at the rear of the pylon, respectively. This flow feature was not observed when the third-order MUSCL reconstruction scheme was applied (not shown). A lateral shift of the hub super-vortex to starboard is identified in Fig. 19 (b), indicating swirl content of the wake. Both subfigures show a strong decrease and rather abrupt ending of the visible vortical structures after the wake was convected out of the fine background grid, which ended directly behind the end of the tail boom. The two main super-vortices, however, were still conserved on the coarser background grid using the WENO scheme. This observation emphasizes the importance of the higher-order spacial reconstruction and a reasonable grid spacing in order to capture and preserve the wake structures appropriately.

Ghee et al. (Ref. 19) examined the wake trajectories at different lateral positions for the "2MRTS" rotor system using the same geometrical rotor specifications at identical operating conditions, as was applied in the ROBIN experiment by Mineck and Alhoff-Gorton (Ref. 6). However, Ghee et al. used a generic fuselage instead of the ROBIN model. Nevertheless, a comparison of the essential wake features should still be reasonable, particularly at locations further away from the immediate influence of the fuselage on the flow. Figure 20 shows the locations of the vortex cores in the wake in two x-z-planes at the lateral station $y/R = -0.8$ in Fig. 20 (a), and $y/R = +0.3$ in Fig. 20 (b). The results of the work of Kenyon (Ref. 20) are plotted as a numerical reference, and the measurements are those of Ghee et al. (Ref. 19).

The experimental data did not allow for the identification of specific vortex locations. Hence, the experiment only provided the path that the vortices in the experimental wake followed. The plotted numerical results, in contrast, show the individual vortex cores and, thus, their locations can be compared directly. Figures 20 (a) and (b) each show two trajectories, representing the vortices trailed from the 180 degree and zero degree azimuthal blade positions. The vortex flow on the retreating side of the rotor at $y/R = -0.8$ was further away from the fuselage and, therefore, the difference between the bodies in experiment and simulation was less significant. Both trajectories of the current results are in close accordance with the experiment in 20 (a), whereas greater deviations from the experiment are observed in Fig. 20 (b). The latter shows a lateral station which was closer to the fuselage, resulting in a greater influence of geometrical shape of the airframe on the flow. Different forms of the helicopter models and the shift of the ROBIN fuselage to the left in the simulation were the two main disparities between experiment and the current setup, which most likely led to the displayed discrepancies. Fur-

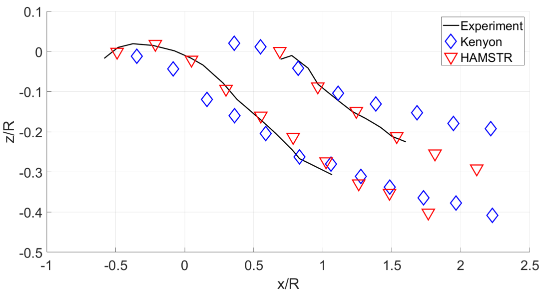

(a) $y/R = -0.8$

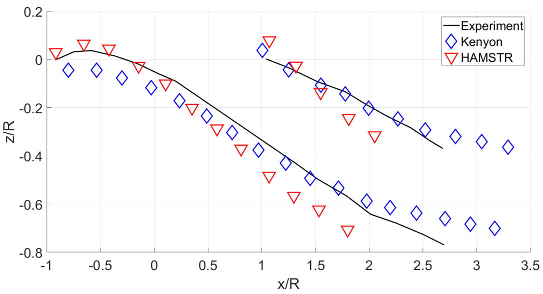

(b) $y/R = 0.3$

Fig. 20: Comparison of wake trajectories at two lateral locations at advance ratio $\mu = 0.151$

thermore, slightly different coning angles and minor flapping motion in the experiment, although minimized by the trim, may have caused additional offset. Comparison with the numerical results from the work of Kenyon showed superior behavior of the current wake solution for all longitudinal stations for the lateral position at $y/R = -0.8$ and for $x/R < 0$ at $y/R = 0.3$. Direct comparison of the vortex core locations showed slightly displaced centers in longitudinal direction, in addition to the offset in z-direction.

Fuselage centerline pressure evaluation The current dynamic pressure coefficients at the advance ratio of $\mu = 0.151$ were compared with the results by Kubrak (Ref. 21), Lee (Ref. 2), Mineck (Ref. 6), O'Brien (Ref. 3), and Steijl (Ref. 22), where available. At the given advance ratio, the rotor wake convected past most of the fuselage and, thus, vortices did not impinge on it. Hence, the main feature that affected the surface pressure in this case was the blade passing event, i.e., a periodic pressure rise due to the blade loading and its impact on the surrounding flow field.

At the front of the fuselage, all assessed numerical results showed similar increased mean pressure levels compared to the experiment with slightly varying amplitudes. As observed in the near-hover case, the experimental amplitudes changed between two peaks due to the differences between the blades. At position D8, shown in Fig. 21, the current results were generally in phase with the experiments and only showed a slight lag of about three degrees. The mean pressure was in accordance with the numerical results of O'Brien and slightly increased compared to the results of Steijl and Kubrak. The latter showed strongly aperiodic behavior, indicating that this solution might not be entirely converged.

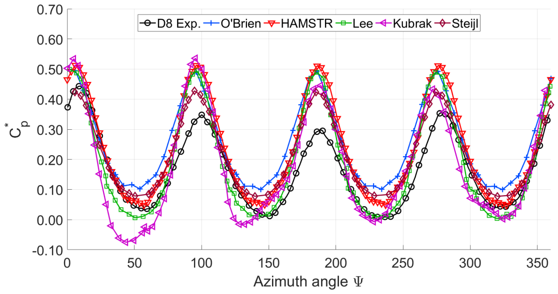

Fig. 21: C_p^* at pressure transducer D8 and $\mu = 0.151$

At position D8, the numerical result of Lee showed the best agreement with the experiment concerning the minimum pressure, whereas the experimental amplitude was matched best by the results of Steijl. However, all numerical results showed pressure peaks that were marginally too high, independent from the applied physical modeling and numerical settings, which both were substantially different in the various numerical studies. The fact that practically all available numerical results, also those that are not shown in the present comparison, overpredicted the mean pressure and the pressure amplitudes, indicates that either better numerical modeling is necessary or that a certain experimental error is present.

The pressure transducers D17 in Fig. 22 and D22 in Fig. 23 represent two opposing ends of the rotor root cutout at 180° and zero degree azimuth angle, i.e., front and aft of the rotor disk, respectively. At both locations, the influence of the blade passing event was strongly decreased compared to the locations on the nose of the fuselage. The effect of the rotor hub and the support structure became more significant at this location and further downstream of it. Since no rotor hub was modeled in the numerical setup, an increased deviation from the experiment was found also in the pressure results.

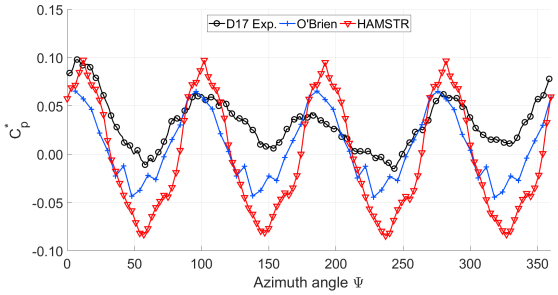

Fig. 22: C_p^* at pressure transducer D17 and $\mu = 0.151$

In contrast to D17, the difference between the current results and the solution found in O'Brien's work was negligible. In fact, the dynamic pressure in the paper by Steijl, who only used a flat plate to model the hub, reproduced the experiment the best. Due to its location on the converging part of the pylon, flow separation and turbulent behavior of the surrounding fluid at transducer D22 is likely. Hence, the $k-\omega$ turbulence model used by Steijl should outperform the Spalart–Allmaras turbulence model used by O'Brien and in the current study, and led to a better agreement with the experiment, because this turbulence model typically deals better with flow separation.

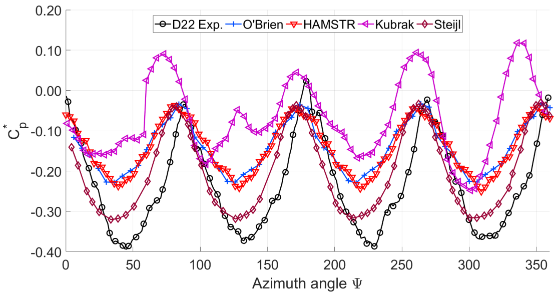

Fig. 23: C_p^* at pressure transducer D22 and $\mu = 0.151$

Similarly to the conditions on the nose, the blade passing effect was the dominant feature observed in Fig. 24. Again, the minimum pressure was overpredicted by almost all numerical simulations, whereas the amplitudes were predicted quite well. Influences from the vortical wake were not present for the presented transducer locations at this advance ratio, since the wake trajectory did not interact with the fuselage. More distinct effects of the tip vortex impinging on the fuselage was only observed for the near-hover case shown previously. However, the experimental evaluation showed a secondary pressure peak after the main cusp. This feature was only resolved with distinctness in the result by O'Brien. The current solution shows a tendency to capture the peak as well, albeit less strong.

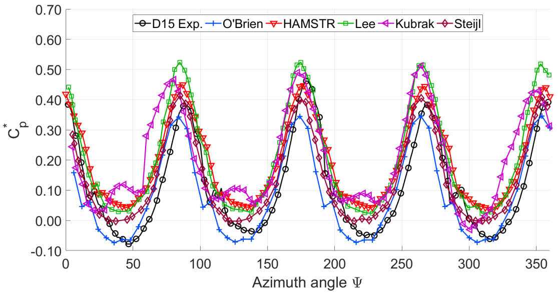

Fig. 24: C_p^* at pressure transducer D15 and $\mu = 0.151$

The steady pressure distribution in Fig. 25 mirrors the observations from the dynamic investigations. The general trend was well captured, however, the mean pressures were consistently overpredicted compared to the experiment. Only the computed pressures at four transducer locations in Fig. 25 reproduced the experimental mean pressures accurately. A significant pressure drop directly before the pylon was not resolved in previous numerical results, whereas the current computation showed the spike. Further evaluations suggested that this peak was caused by a locally bound vortex, with lower pressure in its center.

While the pressures of the current simulation coincided with O'Brien's computational results at the front part of the fuselage, the trends in the pylon section deviated more strongly from each other. A possible explanation might result from a different modeling of the upper support structure. A smaller diameter of the beam was used in the current setup, leading to a smaller deceleration zone of fluid in front of it up to the surface, and a downstream shift of the stagnation point. The following flow through the gap between pylon and support structure might have led to a stronger acceleration and corresponding pressure drop in O'Brien's computation. At the tail, the previous trend followed the experimental findings better than the current computation.

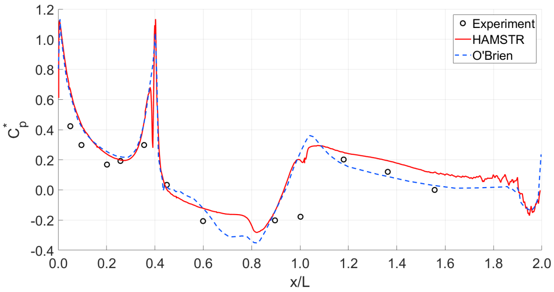

Fig. 25: Fuselage centerline steady C_p^* and $\mu = 0.151$

Both numerical results failed to reproduce the measurement at $x/L = 1.0$, with computational results deviating significantly from the experiment. The coincidence of this position with the tapered end of the pylon, implies that either the modeling of the pressure recovery needs to be reconsidered to better match the experiment or that a greater error in the measurements occurred at this location.

Fuselage circumferential pressure evaluation While the current predicted mean pressure at transducer D19 in Fig. 26 was clearly increased compared to the previous numerical solutions, this was not the case at D25 in Fig. 27. All numerically predicted pressure amplitudes were similar as well.

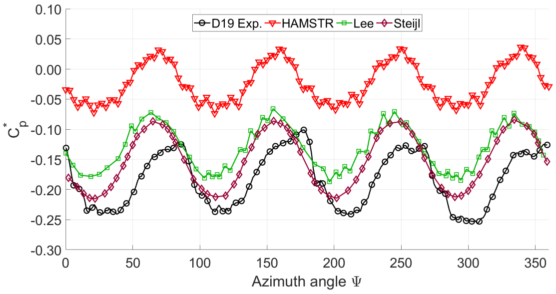

Fig. 26: C_p^* at pressure transducer D19 and $\mu = 0.151$

A phase offset was evident for basically all the circumferential experimental curves compared to any numerical result. The experimental peaks were shifted to greater azimuth angles on port side, while the starboard pressures were shifted in opposite direction. The experimental peaks at D19 showed asymmetric behavior with a smaller secondary peak shortly after the first maximum, which was not reproduced by either of the numerical simulations.

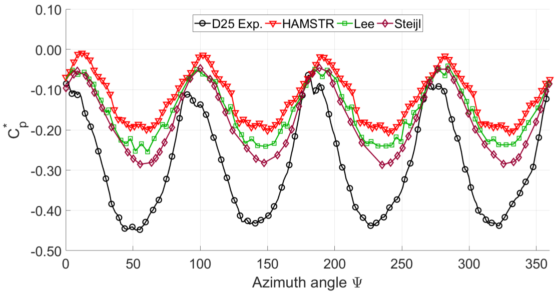

Fig. 27: C_P^* at pressure transducer D25 and $\mu = 0.151$

While the experimental pressure coefficient amplitudes increased from about $\Delta C_P^* = 0.10$ at D19 to $\Delta C_P^* = 0.35$ at D25, the simulations predicted smaller values of about $\Delta C_P^* = 0.25$. In contrast to the pressure measurements on the retreating side at D19, all numerical results failed to reproduce the correct amplitude an mean pressure at D25. Therefore, further improvements in the simulation setup, such as including a hub model, need to be considered.

On the port side location in front of the pylon in Fig. 28 (a), the experimental steady pressure distribution (Ref. 6) was best approximated by Steijl, with the current results showing a similar trend, lying between the various previous numerical curves. While the pressures of Lee and Park (Ref. 23) oscillated strongly on the lower side of the fuselage, this behavior was not observed in the experiment and only in a strongly damped fashion in the current solution.

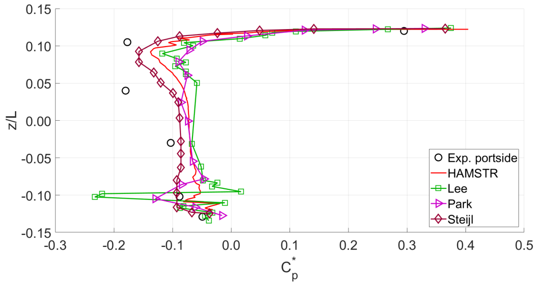

(a) Port

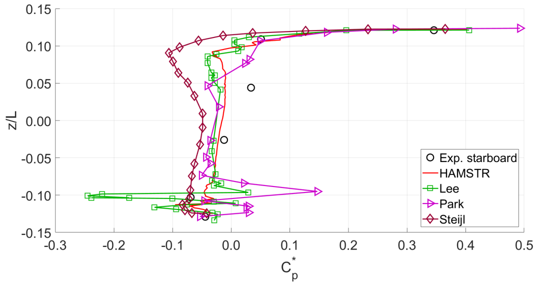

(b) Starboard

Fig. 28: Lateral steady C_P^* at $x/L = 0.35$ and $\mu = 0.151$

The same oscillatory conduct existed at starboard in Fig. 28 (b). In this case, Steijl's result deviated most from the experiment, which now showed positive pressure values on a large part of the upper fuselage. None of the numerical simulations was able to reproduce this trend precisely, and only the lower part of the steady pressure was well reproduced by Steijl's and the current results.

The axial station at $x/L = 1.17$ was directly located behind a rear lower support beam, to which the fuselage was attached. A strong suction pressure peak at the lowest pressure transducers was caused by the negative pressure area behind this support structure. Since none of the numerical setups accounted for this geometrical feature, the negative pressure peak could not be reproduced by either of the simulations.

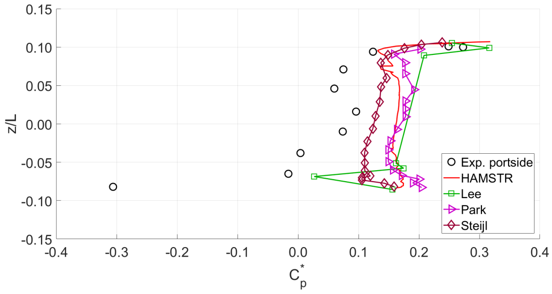

(a) Port

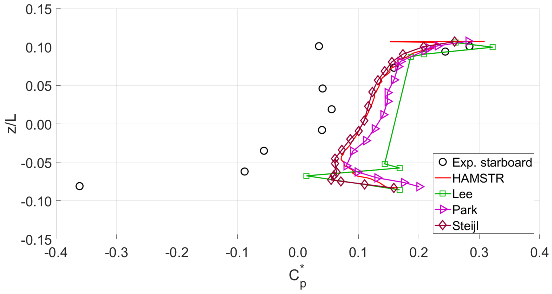

(b) Starboard

Fig. 29: Lateral steady C_P^* at $x/L = 1.17$ and $\mu = 0.151$

5. SUMMARY AND CONCLUSIONS

The recently developed computational RANS solver, HAMSTR, was applied and tested for its ability to simulate the complex vortical rotor wake as well as its interaction with the airframe. An integrated meshing tool used Hamiltonian paths to create artificial structured domains from initially unstructured grids. Two operational conditions for near-hover ($\mu = 0.012$) and medium-speed forward flight ($\mu = 0.151$), defined in previous literature, were reproduced as precisely as possible. Several solution quantities, such as wake appearance, wake trajectory, surface pressure distributions, and surface streamlines were extensively compared with experiments and previous numerical results.

Smaller geometrical adjustments, such as a fuselage yawing angle, coning angles, and a small lateral displacement of the fuselage had little influence on the solution if examined individually. However, a greater combined impact was observed, which included lagging and magnitude variations of the recorded dynamic fuselage surface pressure distributions. The inclusion of an upper support structure proved to be less influential on the solution than expected, while rotor inflow and thrust history were more significantly affected. Both a smaller timestep size and an increased number of subiterations led to a reduced thrust coefficient and, thus, also had an effect on the fuselage pressure levels. Second-order effects, such as secondary pressure oscillations, were only detected with enhanced temporal resolution. In the present study, the intensity of the vortical wake structures was practically independent from the investigated temporal resolution, and instead was strongly affected by the grid spacing and the applied reconstruction scheme. Higher-order reconstruction was advantageous and provided better wake preservation, especially on coarsely partitioned domains.

In general, good agreement of the current results with the experiments and previous numerical studies was found, with the current findings exhibiting mostly superior behavior. When compared with a solution obtained by commercial software, as well as results calculated on fully structured domains, both combined with higher-order turbulence modeling, the current results showed the competitiveness of the applied HAMSTR flow solver. Deviations from previous results and experiments were particularly found in regions of highly turbulent behavior and prevailing flow separation. The lack of a rotor hub and the absence of a lower support structure in the numerical model contributed to deviations in the results from the experiment. Nevertheless, the current solution showed a good balance between computational performance, quality of the solution, and the overall invested time including grid generation.

Future work includes an improved grid generation to account for more complex geometrical features, such as a rotor hub. A finer background grid might be capable of resolving small-scale vortex behavior more precisely, in particular with regard to vortex–surface interactions. Several nested background meshes with optimized shapes and grid spacing and the application of graphics processing units (GPU) will be beneficial in terms of computational resources (Ref. 17). Higher-order interpolation at the overset boundaries between different domains will improve accuracy as well. The coupling of the HAMSTR CFD tool and CSD software to perform a rotor analysis including trim and consideration of elastic blade motion to account for the aeromechanical impact on the blade geometry might further increase the quality of the results.

REFERENCES

[1] Jung, Y. S., Jude, D., Govindarajan, B., and Baeder, J., "Line-Based Unstructured/Structured Heterogenous CPU/GPU Framework for Complex Aerodynamic Flows," American Helicopter Society 73rd Annual Forum, Fort Worth, Texas, May 2017.

[2] Lee, B. S., Jung, M. S., Kwon, O. J., and Kang, H. J., "Numerical Simulation of Rotor–Fuselage Aerodynamic Interaction Using an Unstructured Overset Mesh Technique," International Journal of Aeronautical and Space Sciences, Vol. 11, No. 1, March 2010.

[3] O'Brien, Jr., D., "Analysis Of Computational Modeling Techniques For Complete Rotorcraft Configurations," Dissertation, Georgia Institute of Technology, 2006.

[4] Jung, Y. S., Govindarajan, B., and Baeder, J., "Turbulent and Unsteady Flows on Unstructured Line-Based Hamiltonian Paths and Strand Grids," AIAA Journal, Vol. 55, No. 6, 2017.

[5] Sitaraman, J., and Roget, B., "Solution Algorithm For Unstructured Grids Using Quadrilateral Subdivision and Hamiltonian Paths," AIAA SciTech Forum, 52nd Aerospace Sciences Meeting, National Harbor, Maryland, January 2014.

[6] Mineck, R. E., and Althoff-Gorton, S., "Steady and Periodic Pressure Measurements on a Generic Helicopter Fuselage Model in the Presence of a Rotor," NASA TM 2000-210286, Langley Research Center, Hampton, Virginia, June 2000.

[7] Brazell, M. J., Sitaraman, J., and Mavriplis, D. J., "An Overset Mesh Approach for 3D Mixed Element High Order Discretizations," Journal of Computational Physics, Vol. 322, October 2016.

[8] Roe, P. L., "Approximate Riemann Solvers, Parameter Vectors, and Difference Schemes," Journal of Computational Physics, Vol. 43, No. 2, October 1981.

[9] Rieper, F., "A low-Mach number fix for Roe's approximate Riemann solver," Journal of Computational Physics, Vol. 230, June 2011.

[10] Koren, B., "A Robust Upwind Discretization Method for Advection, Diffusion and Source Terms," Notes on Numerical Fluid Mechanics, Vol. 45, 1993.

[11] Jiang, G. S., and Shu, C. W., "Efficient Implementation of Weighted ENO Schemes," Journal of Computational Physics, Vol. 126, No. 1, June 1996.

[12] Spalart, P. R., and Allmaras, S. R., "A one-equation turbulence model for aerodynamic flows," 30th AIAA Aerospace Sciences Meeting and Exhibit, AIAA Paper 1992-0439, Reno, NV, January 1992.

[13] Spalart, P. R., Deck, S., Shur, M. L., and Squires, K. D., "A New Version of Detached-Eddy Simulation, Resistant to Ambiguous Grid Densities," Theoretical and Computational Fluid Dynamics, Vol. 20, No. 3, May 2006.

[14] Scotti, A., Meneveau, C., and Fatica, M., "Dynamic Smagorinsky Model on Anisotropic Grids," Physics of Fluids, Vol. 9, No. 6, 1997.

[15] Hariharan, N., Egolf, A., and Sankar, L., "Simulation of Rotor in Hover: Current State and Challenges," 52nd AIAA Aerospace Sciences Meeting, National Harbor, MD, January 2014.

[16] Borges, R., Carmona, M., Costa, B., and Don, W. S., "An improved weighted essentially non-oscillatory scheme for hyperbolic conservation laws," Journal of Computational Physics, Vol. 227, No. 6, March 2008.

[17] Jude, D., Lee, B., Jung, Y. S., Petermann, J., Govindarajan, B., and Baeder, J., "Application of a Heterogeneous CFD Framework Towards Simulating Complete Rotorcraft Configurations," American Helicopter Society 74th Annual Forum, Phoenix, Arizona, May 2018.

[18] Elliott, J. W., Althoff, S. L., and Sailey, R. H., "Inflow Measurements Made with a Laser Velocimeter on a Helicopter Model in Forward Flight. Volume 1: Rectangular Planform Blades at an Advance Ration of 0.15," Technical Memorandum, NASA TM 100541, Hampton, VA, April 1988.

[19] Ghee, T., Berry, J., Zori, L., and Elliott, J., "Wake Geometry Measurements and Analytical Calculations on a Small-Scale Rotor Model," NASA TP 3584, Hampton, Virginia, August 1996.

[20] Kenyon, A. and Brown, R., "Wake Dynamics and Rotor–Fuselage Aerodynamic Interactions," Journal of the American Helicopter Society, Vol. 54, No. 1, January 2009.

[21] Kubrak, B. and Snyder, D., "CFD Code Validation of Rotor/Fuselage Interaction Using the Commercial Software STAR-CCM+8.04," 39th European Rotorcraft Forum, Moscow, Russia, September 2013.

[22] Steijl, R. and Barakos, G. N., "Computational analysis of rotor–fuselage interactional aerodynamics using sliding-plane CFD method," 34th European Rotorcraft Forum, Liverpool, England, September 2008.

[23] Park, Y. M., Nam, H. J., and Kwon, O. J., "Simulation of Unsteady Rotor–Fuselage Interactions Using Unstructured Adaptive Meshes," American Helicopter Society 59th Annual Forum, Phoenix, Arizona, May 2003.